

Topological radiation engineering in hyperbolic sonic semimetalsLi-Yang Zheng * and Johan Christensen †*Department of Physics, Universidad Carlos III de Madrid, ES-28916 Leganés, Madrid, Spain* (Received 30 September 2020; revised 3 February 2021; accepted 4 February 2021; published 15 February 2021)

Hyperbolic dispersion enables unprecedented abilities for wave-field engineering which so far chiefly has been realized by man-made metamaterials. Recent classical explorations of topological media and semimetals suggest that these exotic structures may enable a novel route toward hyperbolic sound control. Here, we demonstrate that a three-dimensional acoustic semimetal implementation exhibits nodal lines of hyperbolic shape that are topologically protected due to translational symmetry. The structure comprises a cubic arrangement of crossed hollow channels whose hopping strengths are determined by their cross sections, which facilitate analytically exact prediction of tunable spin-Hall textures. Interestingly, thanks to these nodal signatures of hyperbolic shape, we are able to acquire an array of unusual emission features, spanning from directional collimation to either horizontally or vertically split radiation. We foresee that our findings will provide remarkable opportunities for advanced wave control with hyperbolic and topological attributes.

DOI: [10.1103/PhysRevB.103.064307](https://doi.org/10.1103/PhysRevB.103.064307)**I. INTRODUCTION**

Beyond isotropic structures, engineered metamaterials have enabled the ability to facilitate directional-dependent dispersion relations for superior wave control [1]. For artificial media enabling exotic anisotropic sound-wave characteristics, it boils down to the capacity to acquire a mass density tensor with elements of different values or signs. Particularly, a surge of recent activities have focused on the latter, where metamaterial structures have been designed yielding opposite signs of the effective acoustic density along specific directions [2,3]. Such media with hyperbolic dispersion have been realized by stacking holey plates that entail prominent properties such as negative refraction, focusing, and directional sound emission [4–6].

On a different but at least equally exciting frontier, we find topological insulators, which constitute a paradigm of media and structures to permit and tailor unusual wave guidance [7]. In both time reversal symmetric and broken scenarios or by utilizing structures of specific symmetries to enable certain quantum phases, robust guiding and control of sound waves have been brought forward that abide by the bulk-edge correspondence [8–12]. Beyond this concept, phononic higher-order topological insulators and other so-called zero modes have seen the light of day in many groundbreaking experiments [13–15].

Within the same framework, semimetals have also been studied thoroughly with the aim to unleash even richer topological phases. Dirac and Weyl semimetals belong to the more common groups of these media, but lately many experiments demonstrated highly intriguing and complex interlaced nodal topological features. Particularly, in topological nodal line

semimetals, two bands cross each other along a closed curve called a nodal line [16,18–21]. In such systems, the nodal lines can display a variety of different geometrical characteristics of nontrivial topology [17], leading to exotic intersecting formations such as nodal chains [18,19], nodal knots [20], and Hopf links [21], etc. Engineering the nodal lines to be hyperbolic carries along with it not only a rich avenue for wave physics but further facilitates topological protection to hyperbolic properties originating from the crystal geometry.

In this paper, we demonstrate a hyperbolic media based on an artificially crafted topological acoustic semimetal. As opposed to classical hyperbolic metamaterials, we report unusual and rich wave properties that are associated to the tunable attributes of the spin-Hall textures. Remarkably, we exemplify how unidirectional emission patterns extend over a broad spectral window and are robust against disorder.

II. THEORY AND HYPERBOLIC PROPERTIES

The topological hyperbolic sonic semimetal (THSS) is composed of square-shaped air channels of different cross sections. The unit cell of the THSS is shown in Fig. 1(a), where the differing channels are marked by distinct colors. The distance between consecutive junctions is L . According to the methodology in Refs. [22,23], sound wave propagation in this structure can be exactly mapped to a discreet model comprising the sound pressure at each junction p_A, p_B, \dots, p_H . The coupling of the pressure in neighboring junctions through the air channels is characterized by the coupling coefficients $\alpha, \alpha', \beta, \beta'$, and γ , which are determined through the relative cross sections of the specific guides, see Supplemental Material (SM) [24]. Considering the periodic Bloch condition, the following governing equation is derived [24]:

$$\begin{bmatrix} 0 & \mathcal{D} \\ \mathcal{D}^* & 0 \end{bmatrix} \begin{bmatrix} \mathbf{u} \\ \mathbf{v} \end{bmatrix} = \varepsilon \begin{bmatrix} \mathbf{u} \\ \mathbf{v} \end{bmatrix}, \quad (1)$$

*lzheng@inst.uc3m.es

†johan.christensen@uc3m.es

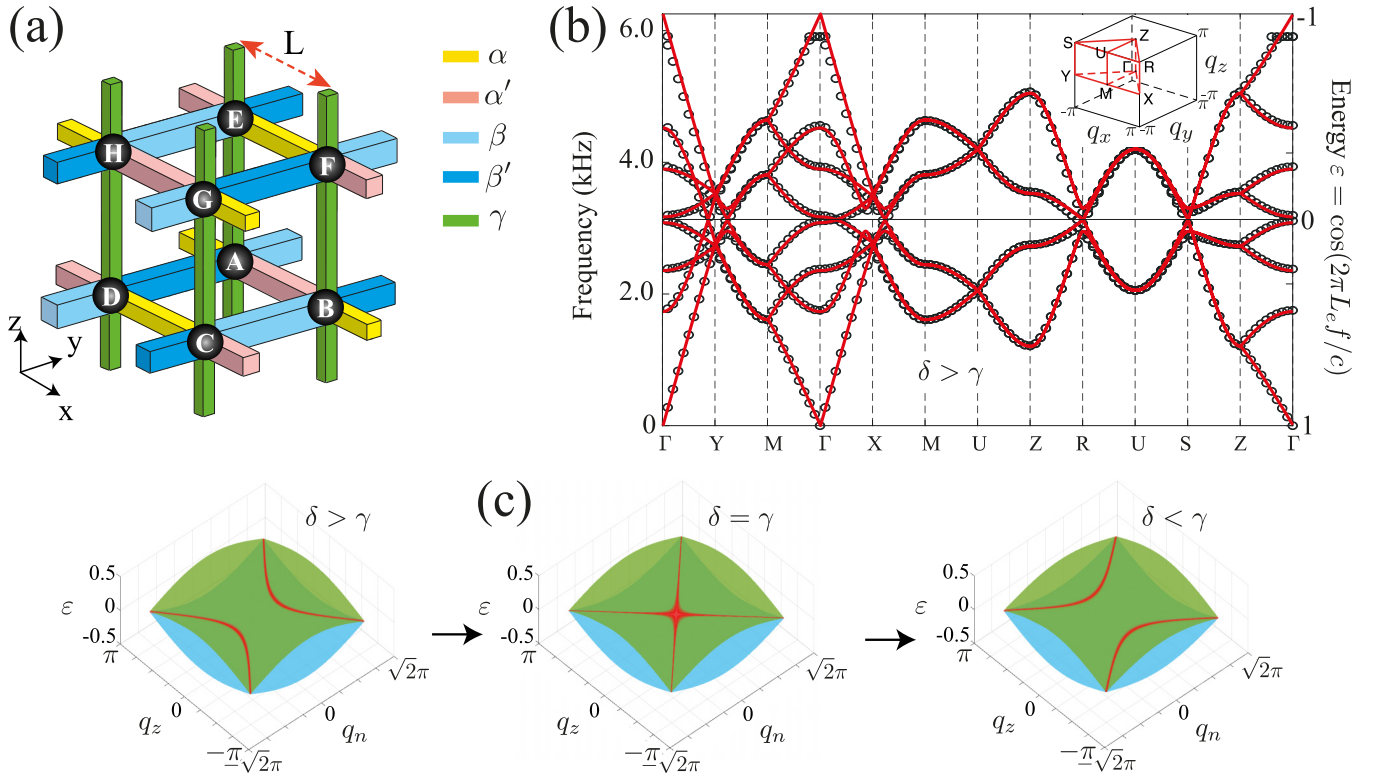


FIG. 1. (a) Schematic view of the unit cell under study. The air channel geometries are labeled by different colors, while their interconnecting junctions are marked as A, B, C, \dots, H . (b) Dispersion curves of the case when $\alpha = \frac{12.5}{45}$, $\alpha' = \frac{10.5}{45}$, $\beta = \frac{8}{45}$, $\beta' = \frac{6}{45}$, and $\gamma = \frac{4}{45}$ ($\delta = \alpha - \beta = \alpha' - \beta' > \gamma$). Red solid lines (black circles) represent the theoretical (numerical) results. The inset shows the Brillouin zone. (c) The nodal lines hyperbola, at zero energy (red), can be tuned to cross a Lifshitz transition at $\delta = \gamma$, i.e., from a type-II ($\delta > \gamma$) to a type-I ($\delta < \gamma$) hyperbolic dispersion. The green and cyan colors represent the surfaces of two bands that cross to form the hyperbolic nodal lines at zero energy.

where $\mathbf{u} = [p_A; p_C; p_F; p_H]$, $\mathbf{v} = [p_B; p_D; p_E; p_G]$. $\epsilon = \cos(2\pi f L_e/c)$ is the energy term with f the sound wave frequency and $c = 344$ m/s the speed of sound in air. L_e is the effective length of two adjacent junctions. $*$ represents the complex conjugate, and $\mathcal{D} = \sigma_0 \otimes (a\sigma_0 + b\sigma_x) + d\sigma_x \otimes \sigma_0$ with $a = \alpha' e^{-iq_x/2} + \alpha e^{iq_x/2}$, $b = \beta' e^{iq_y/2} + \beta e^{-iq_y/2}$, $d = 2\gamma \cos \frac{q_z}{2}$, and σ_0, σ_x are identity and Pauli matrices, respectively. $q_x = 2Lk_x$, $q_y = 2Lk_y$ and $q_z = 2Lk_z$ with the waver vectors k_x, k_y , and k_z along the x, y , and z directions, respectively. The eigenvalue problem from Eq. (1) enables us to determine the acoustic dispersion relation for the THSS. Figure 1(b) illustrates the theoretical dispersion curves (red lines) for experimentally accessible geometrical parameters, i.e., $\alpha = \frac{12.5}{45}$, $\alpha' = \frac{10.5}{45}$, $\beta = \frac{8}{45}$, $\beta' = \frac{6}{45}$, and $\gamma = \frac{4}{45}$, with individual channel widths: $\sqrt{25}$ mm (yellow), $\sqrt{21}$ mm (pink), $\sqrt{16}$ mm (light blue), $\sqrt{12}$ mm (blue), and $\sqrt{8}$ mm (green) [24]. We compare these predictions to both frequency and energy dispersion bands obtained by finite element simulations as presented by black circles shown in Fig. 1(b), which overall display a remarkable agreement.

To unravel the hyperbolic dispersion of the THSS, we strive for complete analytical insight. To acquire this, we fix the coupling coefficients as follows: $\alpha - \beta = \alpha' - \beta' = \delta$, allowing us to map Eq. (1) into a 4×4 matrix equation [24],

$$\begin{bmatrix} \mathcal{H}_+ & 0 \\ 0 & \mathcal{H}_- \end{bmatrix} \begin{bmatrix} s_+ \\ s_- \end{bmatrix} = \epsilon \begin{bmatrix} s_+ \\ s_- \end{bmatrix}, \quad (2)$$

where $\mathcal{H}_\pm = [0, (a-b) \pm d; (a-b)^* \pm d^*, 0]$, and the basis $s_\pm = [s_\pm^\uparrow; s_\pm^\downarrow] = [(p_A - p_C) \pm (p_F - p_H); (p_B - p_D) \pm (p_E - p_G)]$. At zero energy $\epsilon = 0$, which corresponds to the frequency $f = 3067$ Hz, the THSS exhibits nodal lines in the $\mathbf{n}z$ plane, i.e., the $ACEG$ -plane, with a vertical unit vector $\mathbf{e}_\perp = (\frac{1}{\sqrt{2}}, \frac{1}{\sqrt{2}}, 0)$, thus $\mathbf{n} = \mathbf{e}_\perp \times \mathbf{z}$. Based on these geometrical simplifications, the zero determinant of Eq. (2) leads to an exact hyperbolic dispersion relation within the said plane,

$$\frac{\sin^2 \frac{q_n}{2\sqrt{2}}}{\gamma^2} - \frac{\sin^2 \frac{q_z}{2}}{\delta^2} = \frac{\delta^2 - \gamma^2}{\delta^2 \gamma^2}, \quad (3)$$

where q_n is the wave vector along the \mathbf{n} direction. As shown in Fig. 1(c), Eq. (3) indicates that the zero energy nodal lines (isocontour, marked in red) can be tuned from a type-II ($\delta > \gamma$) to a type-I ($\delta < \gamma$) hyperbola with respect to the symmetry axis $q_n = 0$ through a Lifshitz transition at $\delta = \gamma$ [25]. It is noteworthy that the hyperbolic nodal lines are topologically protected due to the translational symmetry [26,27] along the \mathbf{e}_\perp direction: $T_\perp(x, y, z) \rightarrow T_\perp(x+L, y+L, z)$. According to Bloch's theorem, the translation is described as $T_\perp = e^{-i(q_x + q_y)/2}$. Based on the translational symmetry, pseudomirror planes in the THSS can be defined as $M_\perp^2 = T_\perp = -1$ when $q_x + q_y = 2\pi$ [28,29]. This leads to an important implication of the Kramers degeneracy, ensuring the twofold degeneracy of Bloch states at the pseudomirror planes $q_x +$

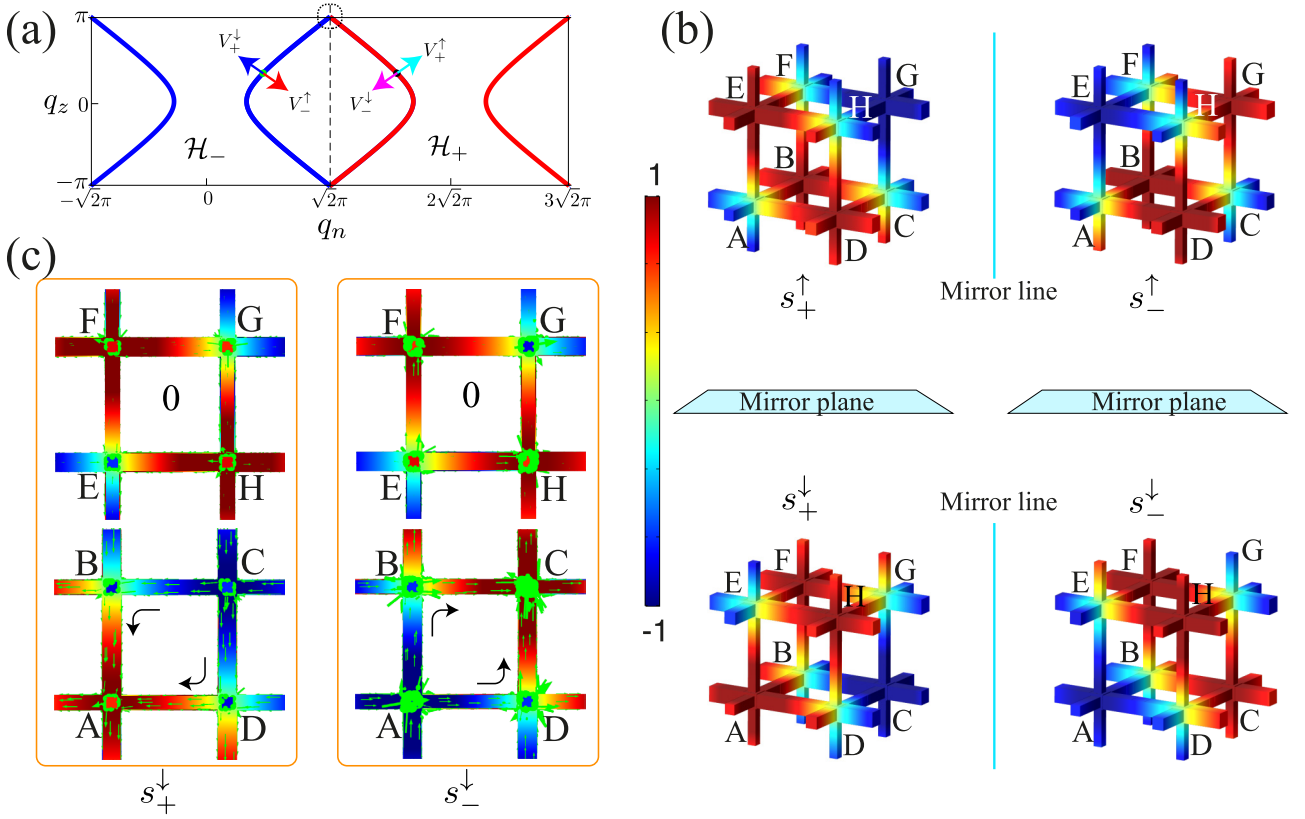


FIG. 2. (a) Hyperbolic dispersion of \mathcal{H}_{\pm} at zero energy for $q_{\perp} = 0$. The dashed line represents a pseudomirror line at $q_n = \sqrt{2}\pi$. The group velocity vectors $V_{\pm}^{\uparrow\downarrow}$, here shown at the green dot and its mirror image (black dot), are normal to the hyperbolic curves and indicate the directions into which power flows. (b) Numerically computed four eigenmodes of the dashed circle marked in (a), which through a mirror transformation can be mapped to each other. (c) Acoustic intensity fluxes of the $s_{\pm}^{\uparrow\downarrow}$ modes in both the $EFGH$ and $ABCD$ planes.

$q_y = 2l\pi$ (l is an integer considering the periodicity), i.e., $q_{\perp} = \sqrt{2}\pi l$ with q_{\perp} the wave vector in the e_{\perp} axis.

To shed more light on the hidden physical properties, in Fig. 2(a) we inspect the type-II hyperbolas of the THSS that are predicted through \mathcal{H}_{+} and \mathcal{H}_{-} at the mirror plane $q_{\perp} = 0$, under the same parameter setting as in Fig. 1(b). The red (blue) nodal lines described by the Hamiltonian \mathcal{H}_{+} (\mathcal{H}_{-}) in Fig. 2(a) are the band degeneracy of a pair of mirror modes $s^{\uparrow\downarrow}$. It originates from the pseudomirror symmetry M_{\perp} that is characterized by the Berry phase [24], which guarantees the nodal lines on the mirror plane to be twofold. Therefore, the nodal lines are protected by the pseudomirror symmetry M_{\perp} with a pair of mirror modes, which can be clearly seen in Fig. 2(b) where the s^{\uparrow} modes are the mirror images of the corresponding s^{\downarrow} modes. Normal to the hyperbolic contours, at the point $(0.623\pi, \pi/3)$ (green dot) and its mirror image (black dot), the group velocity vectors indicate along which direction sound flows, which underlines the unidirectional nature of the $s_{\pm}^{\uparrow\downarrow}$ modes as depicted in Fig. 2(a). To understand the physical meaning of the mirror index freedom- \uparrow (\downarrow), we investigate the acoustic intensity flux of each mirror mode. We found that the mirror index freedom corresponds to the flowing of the flux either in the $EFGH$ plane or the $ABCD$ plane. As examples shown in Fig. 2(c), two eigenmodes of the s^{\downarrow} modes are presented. Surprisingly, it is shown that the acoustic flux (green arrows) of both modes flow across the

$ABCD$ plane only. On the contrary (not shown), the intensity of the s^{\uparrow} modes confine chiefly within the $EFGH$ plane. Further, the hyperbolic index \pm suggests that the THSS also possesses a pair of s_{\pm} modes, which physically are characterized by acoustic intensity fluxes either directed leftward (s_{+} , from junctions C/G toward junctions A/E) or rightward (s_{-} , from junctions A/E toward junctions C/G) as shown in Fig. 2(c), respectively. The topological origin of the s_{\pm} modes is due to pseudo-mirror lines stemming from a translational symmetry $T_n(x, y, z) \rightarrow T_n(x + L, y - L, z)$ within the mirror planes M_{\perp} . Along the \mathbf{n} direction (parallel to mirror planes M_{\perp}), the in-plane translation is written as $T_n = e^{-i(q_x - q_y)/2}$. By defining $\mathcal{L}_{\perp}^2 = T_{\perp} T_n = e^{-iq_x}$, the property $\mathcal{L}_{\perp}^2 = -1$ induces pseudomirror lines \mathcal{L}_{\perp} within the mirror planes M_{\perp} at the positions: $(q_x, q_{\perp}) = [\pi(2t + 1), \sqrt{2}\pi l]$ (l, t are integers). For instance, the dashed line in Fig. 2(a) is a pseudomirror line at the position $(q_x, q_{\perp}) = (\pi, 0)$ ($|q_n| = \sqrt{2}|q_x|$ in this case). As shown in Fig. 2(a), due to the pseudomirror line \mathcal{L}_{\perp} , the two Hamiltonians \mathcal{H}_{\pm} are the mirror images of each other $\mathcal{H}_{+} \rightarrow -\mathcal{H}_{-}$ ([24]) and the eigenmodes of s_{+} mode are the images of the ones of s_{-} mode as presented in Fig. 2(b). Based on the detailed analysis, we can conclude that the hyperbolic nodal lines at $\varepsilon = 0$ are topologically protected by the pseudomirror planes M_{\perp} that stem from the translational symmetry T_{\perp} . This mirror M_{\perp} protection leads to a pair of mirror modes at each hyperbolic curves. Moreover, due to the

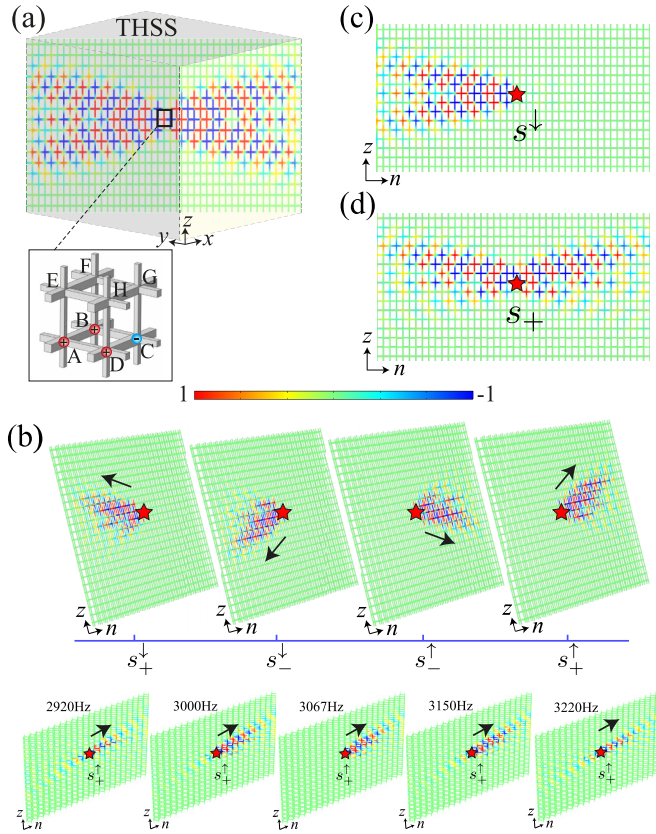


FIG. 3. (a) Sound pressure field distributions in response to an embedded point sources at $f = 3067$ Hz, whose geometrical amplitude arrangement at the junctions enables spin-selective excitation. (b) Emission steering of four unidirectional spin-modes, which are excited by a source (red star). The bottom panel presents the point source excitation of the s_+^\uparrow mode at frequencies as captured. Launching a linear combination of selective spin-modes creates (c) a vertically split (s^\downarrow) and (d) a horizontally split (s_+^\uparrow) radiation pattern.

pseudomirror lines induced by the translational symmetry T_n , each hyperbolic curve contains a mirror counterpart, leading to a pair of hyperbolic nodal lines at each mirror plane M_\perp denoted by the hyperbolic index \pm .

III. TOPOLOGICAL RADIATION

In the following, we aim at harvesting the above detailed 3D spin-Hall textures to facilitate highly unusual acoustic radiation. To do so, we insert point sources at the channel junctions of the sample center with an appropriate amplitude arrangement depicted in the insert of Fig. 3(a). We consider a THSS composed of 21×12 cells in the $\mathbf{n}z$ plane, and infinite in the e_\perp direction. The parameter setting is identical as in Fig. 1(b). By setting the point sources of the finite element simulation to be $[p_A, p_B, p_C, p_D] = [1, 1, -1, 1]$ at $f = 3067$ Hz, the well-known emission pattern is obtained as rendered in Fig. 3(a), displaying how sound is bidirectionally and symmetrically split within the THSS. However, due to the existence of the aforementioned mirror degrees of freedom, there exist four unidirectional spin-Hall selective radiation patterns that we are able to launch. In other words, unlike typical hyperbolic metamaterial sound spread-

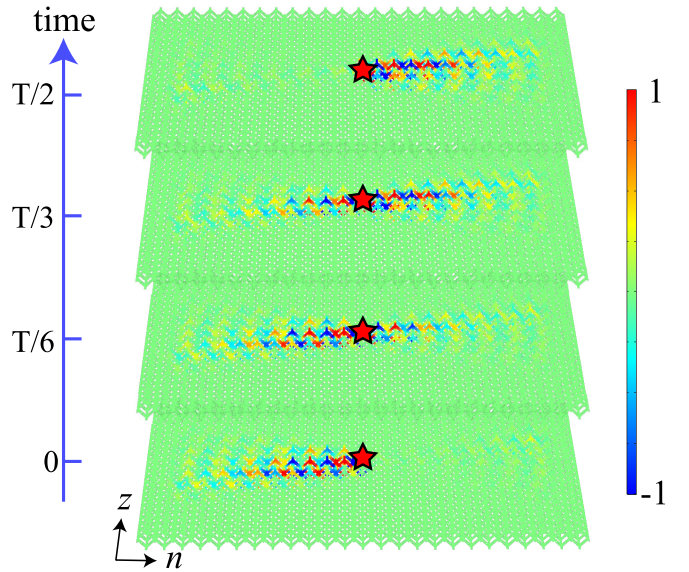


FIG. 4. Time evolution of a spin selective transient excitation, $s_-^\downarrow + is_+^\uparrow$, at $f = 3067$ Hz. During the half cycle, the sound emission is changing direction 180° by virtue of the enforced oscillating between the modes s_-^\downarrow and s_+^\uparrow .

ing, our man-made THSS hosts these peculiar $s_\pm^{\uparrow\downarrow}$ modes, which, once excited, allows for one-way sonic directional radiation. Hence, as illustrated in Fig. 3(b), at zero energy when setting the point sources $[p_A, p_C, p_F, p_H] = [\pm 1, \mp 1, 1, 1]$ sound radiates only left-facing, however, either directed upward (downward) through the s_\pm^\downarrow (s_\pm^\uparrow) mode. On the other hand, acoustic emission facing right can be made possible by tuning the junction amplitudes of the sources to $[p_B, p_D, p_E, p_G] = [1, 1, \pm 1, \mp 1]$, which along the said direction, enables either downward (s_-^\uparrow) or upward (s_+^\uparrow) pointing directional sound. Interestingly, the hyperbolic properties preserve over a considerable bandwidth of ~ 300 Hz. Referring to this, Fig. 3(b) (bottom) illustrates how the s_+^\uparrow mode emission virtually remains the same in a frequency range from 2920–3220 Hz. The great advantage of launching different unidirectional modes by selective excitation has extraordinary radiation possibilities that are robust even in the presence of disorder [24]. Moreover, additional tunability of the acoustic emissivity is given by superimposing various spin-Hall modes. As shown in Fig. 3(c), the linear combination of the s_\pm^\downarrow modes gives rise to collective directional fringes that propagate solely towards the left of the THSS, while the launching of the s_+ waves, due to the linear combination of the $s_\pm^{\uparrow\downarrow}$ modes, leads to the propagation of sound waves facing upwards as presented in Fig. 3(d).

Finally, by introducing a time-varying source to modulate several spin-selective excitations, we are able to cycle in time, among, e.g., the modes $s_-^\downarrow + is_+^\uparrow$ as the simulation in Fig. 4 illustrates. At each half cycle ($T/2$), the emitter (red star) switches between the two unidirectional modes through the respective temporal amplitude arrangement. Hence, both in space and time, we are able to utilize this THSS in routing acoustic signals as desired.

IV. CONCLUSION

In conclusion, we have investigated an acoustic analogy of a three-dimensional topological semimetal, which we designed out of a cubic network of interconnected hollow channels. We found nodal features that are entirely dictated by geometrical means, whose hyperbolic shape can be tuned across an acoustic Lifshitz transition. Analytical predictions confirm that our structure hosts topological modes that are protected due to the translational symmetry. Strikingly, we are able to engineer topological sound radiation that is controlled by the tunable spin-Hall textures, producing a multitude

of unidirectional emission patterns useful for deterministic sound steering in many applications.

ACKNOWLEDGMENTS

J.C. acknowledges support from the European Research Council (ERC) through the Starting Grant No. 714577 PHONOMETA and from the MINECO through a Ramón y Cajal grant (Grant No. RYC-2015-17156). L.Y.Z. acknowledges the support from the CONEX-Plus project (H2020-MSCA-COFUND-2017-UE, Grant No. 2018/00578/012).

-
- [1] S. A. Cummer, J. Christensen and, A. Alu, *Nat. Rev. Mater.* **1**, 16001 (2016).
 - [2] G. W. Milton, M. Briane, and J. R. Willis, *New J. Phys.* **8**, 248 (2006).
 - [3] J. Li and J. Pendry, *New J. Phys.* **10**, 115032 (2008).
 - [4] J. Christensen, and F. J. de Abajo, *Phys. Rev. Lett.* **108**, 124301 (2012).
 - [5] V. M. Garcia-Chocano, J. Christensen, and J. Sánchez-Dehesa, *Phys. Rev. Lett.* **112**, 144301 (2014).
 - [6] C. Shen, Y. Xie, N. Sui, W. Wang, S. A. Cummer, and Y. Jing, *Phys. Rev. Lett.* **115**, 254301 (2015).
 - [7] X. Zhang, M. Xiao, Y. Cheng, M.-H. Lu, and J. Christensen, *Commun. Phys.* **1**, 97 (2018).
 - [8] M. Miniaci, R. K. Pal, B. Morvan, and M. Ruzzene, *Phys. Rev. X* **8**, 031074 (2018)
 - [9] L.-Y. Zheng, G. Theocharis, V. Tournat, and V. Gusev, *Phys. Rev. B* **97**, 060101(R) (2018).
 - [10] M. P. Makwana, N. Laforge, R. V. Craster, G. Dupont, S. Guenneau, V. Laude, and M. Kadic, *Appl. Phys. Lett.* **116**, 131603 (2020).
 - [11] J. Mei, J. Wang, X. Zhang, S. Yu, Z. Wang, and M.-H. Lu, *Phys. Rev. Applied* **12**, 054041 (2019).
 - [12] M. Gao, S. Wu, and J. Mei, *New J. Phys.* **22**, 013016 (2020).
 - [13] X. Zhang, H. X. Wang, Z. K. Lin, Y. Tian, B. Xie, M. H. Lu, Y. F. Chen, and J. H. Jiang, *Nat. Phys.* **15**, 582 (2019)
 - [14] Z. Zhang, H. Long, C. Liu, C. Shao, Y. Cheng, X. Liu, and J. Christensen, *Adv. Mater.* **31**, 1904682 (2019).
 - [15] C.-W. Chen, N. Lera, R. Chaunsali, D. Torrent, J. V. Alvarez, J. Yang, P. San-Jose, and J. Christensen, *Adv. Mater.* **31**, 1904386 (2019).
 - [16] B. Yan, and C. Felser, *Ann. Rev. Condens. Matter Phys.* **8**, 337 (2017).
 - [17] L.-Y. Zheng, X.-J. Zhang, and M.-H. Lu, Y.-F. Chen, and J. Christensen, *Mater. Today Phys.* **16**, 100299 (2021).
 - [18] Q. Yan, R. Liu, Z. Yan, B. Liu, H. Chen, Z. Wang, and L. Lu, *Nature Phys.* **14**, 461 (2018).
 - [19] A. Merkel and J. Christensen, *Commun. Phys.* **2**, 154 (2019).
 - [20] R. Bi, Z. Yan, L. Lu, and Z. Wang, *Phys. Rev. B* **96**, 201305(R) (2017).
 - [21] M. Ezawa, *Phys. Rev. B* **96**, 041202(R) (2017).
 - [22] L.-Y. Zheng, V. Achilleos, O. Richoux, G. Theocharis, and V. Pagneux, *Phys. Rev. Applied* **12**, 034014 (2019).
 - [23] L.-Y. Zheng, V. Achilleos, Z.-G. Chen, O. Richoux, G. Theocharis, Y. Wu, J. Mei, S. Felix, V. Tournat, and V. Pagneux, *New J. Phys.* **22**, 013029 (2020).
 - [24] See Supplemental Material at <http://link.aps.org/supplemental/10.1103/PhysRevB.103.064307> for the theoretical derivations.
 - [25] G. E. Volovik, *Low Temp. Phys.* **43**, 47 (2017).
 - [26] M. Cheng, M. Zaletel, M. Barkeshli, A. Vishwanath, and P. Bonderson, *Phys. Rev. X* **6**, 041068 (2016).
 - [27] S.-P. Kou and X.-G. Wen, *Phys. Rev. B* **80**, 224406 (2009).
 - [28] Y. Ando and L. Fu, *Ann. Rev. Condens. Matter Phys.* **6**, 361 (2015).
 - [29] L. Fu, *Phys. Rev. Lett.* **106**, 106802 (2011).